Journal of Materials Chemistry B

Accepted Manuscript

ROYAL SOCIETY OF CHEMISTRY

www.rsc.org/materialsB

	Stomatology, Ninth People's Hospital Affiliated to Shanghai Jiao Tong University, School of Medicine, Shanghai Key Laboratory of Stomatology, 639 Zhizaoju Road, Shanghai 200011, PR China, Liu, Xuanyong; Shanghai Institute of Ceramics, Chinese Academy of Sciences, ; Shanghai Institute of Ceramics, Chinese Academy of Sciences, State Key Laboratory of High Performance Ceramics and Superfine Microstructure Jiang, Xinquan; Ninth People's Hospital, School of Medicine, Shanghai Jiao Tong University, Department of Prosthodontics; Oral Bioengineering Lab, Shanghai Research Institute of Stomatology, Ninth People's Hospital Affiliated to Shanghai Jiao Tong University, School of Medicine, Shanghai Key Laboratory of Stomatology, 639 Zhizaoju Road, Shanghai 200011, PR China,

Strontium delivery on topographical titanium to enhance bioactivity and osseointegration in osteoporotic rats

Jin Wen[a, b,1], Jinhua Li[c,1], Hongya Pan[b], Wenjie Zhang[a,b], Deliang Zeng[a,b], Lianyi Xu[a,b], Qianju Wu[a,b], Xiuli Zhang[b], Xuanyong Liu[c,*] and Xinquan Jiang[a,b,*]

[a] Department of Prosthodontics, Ninth People's Hospital affiliated to Shanghai Jiao Tong University, School of Medicine, 639 Zhizaoju Road, Shanghai 200011, China.

[b] Oral Bioengineering Lab, Shanghai Research Institute of Stomatology, Ninth People's Hospital Affiliated to Shanghai Jiao Tong University, School of Medicine, Shanghai Key Laboratory of Stomatology, 639 Zhizaoju Road, Shanghai 200011, China.

[c] State Key Laboratory of High Performance Ceramics and Superfine Microstructure, Shanghai Institute of Ceramics, Chinese Academy of Sciences, Shanghai 200050, China.

Corresponding Authors:

Prof. Xinquan Jiang

Department of Prosthodontics, Ninth People's Hospital affiliated to Shanghai Jiao Tong University, School of Medicine, 639 Zhizaoju Road, Shanghai 200011, China.

E-mail: xinquanj@aliyun.cn

Tel.: +86 21 63135412. Fax: +86 21 63136856.

Prof. Xuanyong Liu

State Key Laboratory of High Performance Ceramics and Superfine Microstructure, Shanghai Institute of Ceramics, Chinese Academy of Sciences, Shanghai 200050, China.

E-mail: xyliu@mail.sic.ac.cn

Tel.: +86 21 52412409. Fax: +86 21 52412409.

[1] These authors contributed equally to this work.

Abstract

Osseointegration remains a major clinical challenge in osteoporotic patients. Strontium (Sr) has been shown to be a significant therapy to favor bone growth by both increasing new bone formation and reducing bone resorption. In this study, we attempt to chemically functionalize Ti implants by micro-arc oxidation, alkali treatment and ion exchange. This functionalized Ti surface possessed a hierarchical topography with Sr incorporation, which can release Sr ions at a slow rate. To our knowledge, this work is the first to use this type of Sr-doped Ti surface to address osteoporotic bone mesenchymal stem cells (BMSCs) in the dual directions of bone regeneration, bone formation and bone resorption. The modified surface was demonstrated to remarkably enhance the adhesion, spreading, and osteogenic differentiation of BMSCs *in vitro*. The effect of the wash-out solution from various groups on osteoporotic BMSCs was also investigated. The Sr-doped group can improve the ALP activity and osteogenic gene expression. Moreover, the Sr-doped group and the wash-out solution show the most inhibition in osteoclast formation and maturation. Furthermore, the increased bioactivity of the hierarchical structure was also confirmed with the ovariectomized rat femur model in vivo. The outcome of fluorescence labeling, histology and histomorphometric analysis demonstrated a significant promotion of osseointegration in ovariectomized rats. Altogether, the experimental data indicate that the fabrication of a Sr-doped hierarchical Ti surface is a meaningful attempt to incorporate the Sr nutrient element into Ti-based implants, and it is expected to be exploited in developing better osseointegration for

osteoporotic patients.

Keywords: titania; strontium; stem cells; osteoclasts; osseointegration; ovariectomy

1. Introduction

Osteoporosis is a common major disease that often does great harm to human health due to the specific high morbidity, mortality, and disability rates and high cost of living in addition to low quality of life. Osteoporosis is characterized by low bone mass and the microarchitecture deterioration of bone tissue, which can easily lead to enhanced bone fragility in elderly people, especially in postmenopausal women.[1] Many researchers have reported that poor bone quality has a great influence in the rate of osseointegration when compared to healthy individuals.[2] When these patients seek implant treatment, the outcome does not reach a desirable state due to the unmatched implant load and limited osteoinductivity, which may result in a reduced effect or implant failure. Often, the patients will suffer the dual loss of dental fixation and inflammation-related bone loss.[3]

To address the above problems, research has increasingly focused on the substitution of bioactive elements and surface modification to help speed and increase osseointegration between an implant surface and the surrounding bone tissue in osteoporotic patients. Strontium (Sr) is reported to have a beneficial effect in osteoporotic patients, and strontium ranelate (SR) has been authorized by the FDA as an effective drug to treat osteoporosis.[4] Numerous *in vitro* and *in vivo* studies have demonstrated that Sr is one of the most potent bioactive element candidates for bone metabolism. Sr has been shown to possess a high potential to stimulate the proliferation and differentiation of osteoblast cells, inhibiting the activity and differentiation of osteoclasts *in vitro* and promoting bone healing by both increasing

new bone formation and reducing bone resorption.[5-7] Recent studies have attempted to take advantage of the stimulatory effects of Sr on bone healing by incorporating it into various bone implantation biomaterials. Many researchers doped Sr element into bioglasses or bioceramics to study the effect on bone regeneration.[8-12] Other studies used the Sr-substituted biomaterials to address osteoporotic bones and found significant enhancement in bone formation.[13, 14] Researches have also been conducted to establish a unique sustained release platform on a titanium surface to release Sr ions.[15, 16] These studies were designed to achieve the slow release of Sr ions from an implant surface, which could be a significant challenge for surface modification. There were also some works that incorporated Sr directly into Ti surface and reported enhanced bone forming effects because of its positive effects on surface chemistry.[17-19] Thus, it is expected that Sr incorporation into implant surfaces could be an effective approach to enhance the osteoconductivity of bone-interfacing implants. If so, it is also expected that a Sr-contained implant surface would improve implant osseointegration in ovariectomized rats.

However, little research has been conducted to establish a unique sustained release platform on a titanium surface to release Sr ions; managing to achieve the slow release of Sr ions from an implant surface could be a significant challenge for surface modification. Meanwhile, Ti-based implants have an inherent limitation due to their low bioactivity and osteoinductive capacity to induce bone apposition. Based on the above perspectives, we propose that more attention should be paid to modifying the implant surfaces to be as osteoconductive as possible so that the implants have the

best chance to achieve fast osseointegration and promote bone ingrowth.

Extensive studies have focused on modifying the implant surface topography (morphology) and surface chemistry (composition) to gain an enhancement by functionalizing titanium surface, increasing clinical success rates and shortening the healing period.[20] A series of interactions will occur between the implant surface and the physiological environment after implantation into the human body. It is evident that the implant surface plays a key role when biomedical materials/devices respond to the physiological environment. The performance of artificial implants mainly depends upon the surface characteristics such as topography and composition.[21] From the perspective of bionics, cell functions would be positively enhanced by constructing hierarchical structure containing micro- and nanosized parts on implant surfaces to better mimic the architecture of the natural extracellular matrix.[22, 23] There have been some attempts to prepare such biomimetic micro/nanotopographies for promising applications in tissue engineering scaffolds[24-26] and implant surfaces[27-29], implying a huge potential of biomimetic topographical modification for bone implants. Some works also investigated the osteogenic effect of Sr in Ti implants with hierarchically complex surface morphology.[29-32] However, to our knowledge, it is rare to use Sr-substituted implants together with micro/nanotopography to investigate the bone formation and osseointegration in osteoporotic bones in current research, though there have been some previous studies of Sr-doped implants *in vivo*.[33-35] Therefore, our interest was aroused and we were inspired to design this study due to the possibility of the Sr element stimulating osteogenesis as well as the possibility that the

micro/nano surface improving cell–material interactions could have a synergetic effect on promoting osseointegration and bioactivity.

In this study, a hierarchical hybrid topography was produced on a titanium surface by micro-arc oxidation and alkali treatment, followed by ion exchange to introduce strontium element. This Sr-doped Ti implant was designed to explore the effects of surface composition and surface morphology on ovariectomized rats to study how to enhance the osseointegration in osteoporosis patients over the long term. The modified Ti implants were used to address osteoporotic bone mesenchymal stem cells (BMSCs) and osteoclasts *in vitro* and further inserted into the femur model of ovariectomized rats for 8 weeks to evaluate osseointegration *in vivo*.

2. Materials and methods

2.1. Sample fabrication and modification

Commercially pure Ti foils (Grade 1, purity > 99.85 wt%) with sizes of 10 mm × 10 mm × 1 mm or 20 mm × 20 mm × 1 mm were ground, polished to a shiny surface texture, and then ultrasonically cleaned with ethanol and ultrapure water several times to acquire a clean and homogeneous surface, followed by drying. In the animal experiments, Ti rods (Grade 1) with a diameter of 2 mm and length of 7 mm were employed. TiO_2 coatings were prepared on Ti surfaces by micro-arc oxidation in calcium/phosphate-containing electrolyte with calcium acetate monohydrate ($C_4H_6O_4Ca{\cdot}H_2O$), glycerophosphate disodium salt pentahydrate ($C_3H_7Na_2O_6P{\cdot}5H_2O$). After MAO, alkali treatments were conducted on the TiO_2 coatings. Briefly, each

MAO-treated Ti foil was immersed in NaOH aqueous solution (10 M) in a Teflon-lined reaction vessel at 120 ºC for 6 hours. After the reaction vessel naturally cooled to room temperature, the Ti foils were gently rinsed with deionized water and then exchanged in HCl (0.1 M) or $SrCl_2$ (0.1 M) aqueous solution for 2 hours.[19] Then, the Ti foils were rinsed to neutral with deionized water and dried in ambient atmosphere. The final specimens were denoted as Ti, TiO_2, AT-TiO_2 and Sr-TiO_2, respectively.

2.2. Surface characterization

The surface morphology was characterized by field-emission scanning electron microscopy (FESEM; Magellan 400, FEI, USA) equipped with an energy-dispersive X-ray spectrometer (EDS). The crystallinity of the coatings was determined using an X-ray diffractometer (XRD; D/Max, Rigaku, Tokyo, Japan) fitted with Cu Kα (λ = 1.541 Å) source at 40 kV and 100 mA in the range of 2θ = 15º ~ 80º with step size of 0.02º. Phase identification was performed with the help of the standard JCPDS database. In the X-ray diffraction experiment, the glancing angle of incident beam against the specimen surfaces was fixed at 1º. The chemical components and chemical states of sample surfaces were investigated by X-ray photoelectron spectroscopy (XPS; PHI 5802, Physical Electronics Inc., Eden Prairie, MN) with Mg Kα (1253.6 eV) source.

2.3. Ion release measurement

The TiO_2, AT-TiO_2 and Sr-TiO_2 samples were soaked in 10 ml Dulbecco's Modified Eagle's medium (DMEM, Gibco, USA) at 36.5 ºC for 1, 4, 7 and 14 days successively. At the end of each incubation, the leaching liquid was collected and the release amounts of Ca, P, Sr and Ti (IV) ions were determined by inductively-coupled plasma mass spectrometry (ICP-MS; Nu Instruments, Wrexham, UK).

2.4. Osteoporotic animal model

Sixteen female Sprague-Dawley rats aged 3 months and weighing approximately 200 g were included. All the animals used were obtained from the Ninth People's Hospital Animal Center (Shanghai, China) and the experimental protocol was approved by the Animal Care and Experiment Committee of Ninth People's Hospital. In this study, the surgical procedures used to build the OVX osteoporotic animal model included making a small single dorsal incision in each side, freeing the subcutaneous connective tissue and making an incision on the underlying muscle, then finding the ovary around the oviduct and removing it with severing the oviduct.[36]

2.5. OVX BMSCs isolation and culture

Total BMSCs were isolated from ovariectomized rats with an average weight of 200 g (OVX BMSCs).[31, 32] Both ends of the rat femora were cut off at the epiphysis and the marrow was quickly flushed out with Dulbecco's Modified Eagle's medium (DMEM) (Gibco BRL, Grand Island, NY, USA) with 10 % fetal bovine serum (FBS)

(Hyclone, USA), 23 mM $NaHCO_3$ (Gibco Biocult, Paisley, U.K.) and antibiotics (100 U/ml streptomycin sulfate and 100 U/ml penicillin), containing 200 U/ml heparin (Sigma, USA). BMSCs were cultured as previously described.[37]

Bone marrow was mixed with 10 ml DMEM and then centrifuged at 1000 rpm for 15 min. Nucleated cells were suspended in DMEM containing 10 % (v/v) FBS. Primary cells were incubated at 37 ºC in a humidified atmosphere of 95 % air and 5 % CO_2. After 96 hours, non-adherent cells were discarded and adherent cells were cultured. Fresh culture medium was replenished once every three days. After 14 days when the culture dishes reached 80-90 % confluence, the cells were detached and serially sub-cultured into the new dishes at a density of 10 million cells per 100 mm culture dish (Falcon, BD Biosciences, USA) new dishes at density of 1.0×10^5 cells/ml using trypsin/EDTA (0.25 % w/v trypsin, 0.02 % EDTA). Cells at passage 2~4 were used in the following *in vitro* experiments.

2.6. OVX BMSCs growth

The cell proliferation activity of the OVX BMSCs on different samples was evaluated by a CCK8 assay. Initially, a density of 2.0×10^4 cells were seeded onto each flat titanium sample in a 24-well plate. After 1, 4 and 7 days of culture, CCK8 solution with volume of ~10 % of culture medium was added for 1 hour at 37 °C to react with the cells before refreshing all the culture medium of the plates. The absorbance was then measured at 490 nm using an ELX ultra microplate reader (BioTek, Winooski, VT). All experiments were performed in triplicate. The adhesion

and spreading of OVX BMSCs cultured on the different samples were examined after 12 and 24 hours of culture. The cytoskeleton was stained with fluorescein isothiocyanate-phalloidin (FITC-Phalloidin, Sigma, USA) and the cellular nuclei were counterstained with 4', 6-diamidino-2-phenylindole dihydrochloride (DAPI, Sigma, USA) after fixed in 4 % paraformaldehyde.

2.7. ALP and ARS activity assay

OVX BMSCs were seeded on each titanium sample in 24-well plates at a density of 5×10^5 cells. Alkaline phosphatase (ALP) staining was performed according to the manufacturer's instructions (Beyotime, China) at 7 days. Mineral deposits were then evaluated at 14 days by alizarin red S (ARS) staining. To measure ALP, cells were rinsed three times with phosphate-buffered saline (PBS); the cells were fixed and stained using an ALP kit. For the ARS activity assay, cells were washed twice with PBS and fixed in 95 % alcohol for 15 min. 0.1% ARS solution was used for staining, and 10 % cetylpyridinium chloride (Sigma) was used for desorbing the stained samples for the quantification. The OD values for absorbance of the eluent were determined at 590 nm. Total protein values were measured using the Bio-Rad protein assay kit at 630 nm. The results were normalized and presented as OD values per mg of total protein.

2.8. RNA isolation and real-time PCR analysis

Total cellular RNA extraction was performed with TRIzol reagent (Invitrogen)

according to the manufacturer's instructions at day 1 and day 4. Two micrograms of total RNA was used as the template for reverse transcription with a Prime-Script™ RT reagent kit (Takara Bio, Shiga, Japan). The expression of osteogenic genes, including runt-related transcription factor-2 (Runx-2), osteocalcin (OCN), bone morphogenetic protein-2 (BMP-2), and vascular endothelial growth factor (VEGF) were measured using a real-time PCR system (Bio-Rad) with SYBR GREEN PCR Master Mix. The primer sequences for these genes are listed in **Table 1**. Gene-specific primers were synthesized commercially (Shengong Co., Ltd. Shanghai, China). All mRNA values were normalized against the housekeeping gene, glyceraldehyde-3-phosphate dehydrogenase (GAPDH) expression, quantified by the ΔΔCT method.

2.9. Immunofluorescence

The OVX BMSCs were seeded on titanium samples at a density of 5×10^5 cells/ml for 4 days to detect the osteocalcin (OCN) expression, and then the samples were washed with PBS three times and fixed in 4 % paraformaldehyde for 30 min. The cells were then permeabilized with 0.1 % triton X-100 for 30 min and blocked in 10 % goat serum for 1 hour at room temperature. A specific primary antibody targeting osteocalcin (Abcam, USA) was added at 1:100 dilutions and co-incubated overnight at 4 ℃. DyLight 488-conjugated anti-mouse IgG antibody (Boster, CHINA) at 1:100 dilutions was used in the dark. The specimens were observed using a confocal laser scanning microscope (CLSM; Leica TCS Sp2 AOBS, Germany) while

cellular nuclei were contrast-labeled with DAPI (Sigma, USA).

2.10. Investigation on extracts

The different titanium samples in 15 ml tubes with 10 ml DMEM culture medium were incubated under the same conditions as above. The wash-out solution were collected and refreshed with DMEM every 3 days. After 14 days of incubation, the accumulated ion concentrations of Ca, P and Sr were measured by ICP-MS. The collected extracts were supplemented with 10% FBS for the following cell culture experiments.

2.11. Osteoclast differentiation

The cells on the titanium samples and plates with extracts went through RNA isolation and real-time PCR analysis for Cathepsin K (CTSK) and TRAP gene expression. The primer sequences are in **Table 1**. To detect the protein expression, the cells on the titanium samples were used for CTSK expression. The cells were permeabilized with 0.1% triton X-100, fixed for 30 min, blocked with 10% rabbit serum at room temperature and incubated with primary antibody Anti-Cathepsin K (Abcam, USA) at 2 μg/ml for 30 minutes at 25 °C. DyLight 488-conjugated anti-rabbit IgG antibody (Boster, CHINA) at 1:100 dilutions was used while cellular nuclei were contrast-labeled with DAPI. The cells cultured in the extracts fabricated by the medium were used to test the tartrate resistant acid phosphatase (TRAP) activity; a staining kit from Sigma was used for this experiment. Once wells were

fixed after being washed to remove the non-adherent cells, Naphtol Anilid-Acid-Biphosphate (Sigma, USA) with Fast Garnet GBC (Sigma, USA) according to the protocol were added to the wells for 30 min until the staining came out.

2.12. Animal experiments

Twelve weeks after bilateral ovariectomy, all rats were randomly divided into four groups (8 animals per group): (i) Ti group (n=8); (ii) TiO_2 group (n=8); (iii) AT-TiO_2 group (n=8); (iv) Sr-TiO_2 group (n=8). Surgical procedures were performed on SD rats under sterile conditions as described previously.[38] Briefly, approximately a 10 mm longitudinal incision was made along the lateral side of the extensor mechanism around the knee joint, a pilot hole was drilled through the intercondylar notch and distal femoral metaphysic, and the implants were inserted. After the operation, all rats received antibiotic and analgesic injections intramuscularly for three postoperative days.

2.13. Sequential fluorescent labeling

A polychrome sequential labeling method as shown in our previous study[39] was performed to label the mineralized tissue and evaluate the time course of new bone formation and remodeling. At 2, 4 and 6 weeks after the operation, the animals were intraperitoneally administered 30 mg/kg alizarin red S (AL; Sigma), 25 mg/kg tetracycline (TE; Sigma) and 20 mg/kg calcein (CA; Sigma). At 8 weeks, the rats

were sacrificed and immersed in formalin. The specimens were dehydrated gradually in ascending concentrations of alcohols from 75 % to 100 %, and were finally embedded in polymethyl methacrylate (PMMA). The specimens were cut into 150 μm thick sections using a Leica SP1600 saw microtome (Leica, Nusseloch, Germany), and subsequently ground and polished to a final thickness of approximately 50 μm.

2.14. Histological and histomorphometric observation

To quantitate the bone formation and mineralization in the raised area, sections were observed for fluorescence labeling TE, AL and CA under Leica CLSM. Excitation/emission wavelengths for each of the fluorescence were as follows: 405/580 nm (TE, yellow), 543/617 nm (AL, red) and 488/517 nm (CA, green). The percentage of single fluorochrome staining was calculated as previously described; it represented the bone formation and mineralization at the time 2, 4 and 6 weeks after the operation. The fluorochrome staining of the five areas at the top, mesial, center, distal and bottom for each section as described in our previous study was scanned. The area of new bone formation was calculated using a personal computer-based image analysis system (Image-Pro Plus). The sections were further stained with van Gieson's picrofuchsin for histological observation and histomorphometric analysis after fluorescent analysis.

2.15. Statistical analysis

All data were expressed as means ± standard deviation. Statistical significance

was assessed for the above assays was performed by ANOVA and SNK post hoc or Kruskal-Wallis nonparametric procedure followed by Mann-Whitney U test for multiple comparisons based on the normal distribution and equal variance assumption test, using SPSS v.10.1 software (IBM SPSS, Armonk, New York, USA). (*, $p < 0.05$ and **, $p < 0.01$)

3. Results

3.1. Sample characterization

Figure 1a-b shows the surface morphology of metallic Ti after grinding and polishing (control group). After micro-arc oxidation treatment, a rough microporous texture is produced on the metallic Ti surface, as shown in **Figure 1c**. These micropores are well separated from one another and homogeneously distributed over the coating surface. Nevertheless, at high magnification, the coating surface presents a relatively flat topography (see the inset of **Figure 1d**). In regard to the phase composition, the surface coating is chiefly composed of anatase TiO_2, based on the XRD pattern in **Figure S1**.[40] After the alkali treatment and subsequent protonation, homogenous microcracks emerge on the coating surface at low magnification in **Figure 1e**, while unique nanoridge topography appears at high magnification (**Figure 1f**). **Figure 1g** shows that, after Sr ion exchange, the low-magnification morphology of the coating surface formed by micro-arc oxidation and alkali treatment remains intact. This situation can be further demonstrated by the similar high-magnification nanoridge topography in **Figure 1h**. With regard to phase composition, the protonated

and Sr-exchanged coatings both contain the main phase of anatase TiO_2. Furthermore, the attributive diffraction peaks of the titanate phase also appear in the XRD pattern, especially for the Sr-exchanged coating (**Figure S1**).[41] More details on the microcrack formation will be discussed in the next section.

Figure 2a-c shows the XPS full spectra acquired from the surfaces of samples TiO_2, AT-TiO_2 and Sr-TiO_2. According to the XPS analysis results, after micro-arc oxidation (MAO) treatment, oxygen (O), calcium (Ca), phosphorus (P) and titanium (Ti) elements are detected on the TiO_2 coating (**Figure 2a**). As shown in **Figure 2b**, after alkali treatment and subsequent protonation, sodium ions (Na^+) are removed from the titanate layer.[19] In addition, the Ca and P elements suffered some loss. After ion exchange in $SrCl_2$ solution, the Sr element is also detected on sample Sr-TiO_2, with a content of 6.87 at% (**Figure 2c**). A further high-resolution XPS analysis is performed for sample Sr-TiO_2, as shown in **Figure 2d-f**. With regard to the Ca 2p XPS spectrum (**Figure 2d**), three peaks are fitted with the predominant ones at 347.1 eV and 350.6 eV attributed to Ca 2p in $Ca_3(PO_4)_2$ and the third one at 347.5 eV assigned to $CaHPO_4$.[42, 43] As for the P 2p spectrum (**Figure 2e**), the two peaks located at 133.6 eV and 132.3 eV are in accordance with the P–O bonds in PO_4^{3-} and HPO_4^{2-}, respectively.[42, 44] In regard to the Sr 3d spectrum (**Figure 2f**), the doublet peaks at 133.6 eV and 135.3 eV correspond to Sr $3d_{5/2}$ and Sr $3d_{3/2}$ in strontium titanate, respectively.[19]

Figure 2g-i shows the release features of Ca, P, Sr and Ti(IV) ions from the surfaces of samples TiO_2, AT-TiO_2 and Sr-TiO_2 after immersion in DMEM for 1, 4, 7

and 14 days, correspondingly. Within the immersion duration, Ca (**Figure 2g**) and P (**Figure 2h**) ions are sustainably released from each of the sample surfaces, especially for the sample Sr-TiO_2, which shows a significant uptrend, while AT-TiO_2 releases the least. After Sr incorporation, the Sr-TiO_2 coating can continuously release Sr ions into the surrounding DMEM (**Figure 2i**). It can be seen that the release characteristics of these ions are consistent with the surface XPS analysis in **Figure 2a-b**. Meanwhile, the Ti (IV) ions do not dissolve congruently with the Ca, P and Sr ions as their dissolution is not detected from each sample. More details on these release features will be discussed in the next section. As the Sr elements exist in strontium titanate,[19] **Figure S2** depicts the corresponding EDS mapping of Sr, O and Ti elements on Sr-TiO_2 coating, which demonstrates the uniform distribution of these elements on the coating.

3.2. Cell spreading and proliferation

Estimating the effects of the synergetic strategies on the cell proliferation rate is performed by CCK8 assay. The assay is performed after 1, 4, and 7 days to investigate cell proliferation on the samples. From the results in **Figure 3a**, the cell proliferation is significantly influenced by the surface topography and chemistry. Samples Ti and TiO_2 show higher proliferation rates and cell vitality than samples AT-TiO_2 and Sr-TiO_2, in agreement with our recent observation.[45] To check the effects of the surface modification on cell adhesion and spreading, OVX BMSCs cultured on the different samples were examined after 12 and 24 hours of culture, as

shown in **Figure 3b.** The results show that all the samples can serve as platforms for cell adhesion and spreading. It is obvious that the OVX cells spread out more extensively on all the samples at 24 hours than at 12 hours.

3.3. ALP and ARS activity

As an early marker of BMSCs differentiation, ALP is measured on day 7 to assess the osteogenic differentiation potential of OVX BMSCs cultured on the samples. From the results in **Figure 4a**, it is remarkable that the most intense ALP staining was found in samples Ti and TiO_2. Between the modified groups, the intensity of staining became much stronger after Sr substitution. ARS staining was also performed to evaluate the calcium nodule formation in the samples. Remarkably, sample Sr-TiO_2 showed the greatest extent of all the groups. The extent of the staining increased from sample Ti to sample Sr-TiO_2. The data **Figure 4b** displays are in accordance with the staining results. The semi-quantitative results share a similar trend with the staining outcome (including ALP and ARS staining) throughout the observation period.

3.4. OVX BMSCs differentiation

To further investigate the effect of strontium and topography on OVX BMSCs differentiation on the molecular level, a quantitative real-time PCR assay was performed to detect the key osteogenic-related markers, including the runt-related transcription factor 2 (Runx2), osteocalcin (OCN), bone morphogenetic protein II

(BMP-2), and vascular endothelial growth factor (VEGF) after the cells were cultured for 1 and 4 days. Overall, the samples AT-TiO_2 and Sr-TiO_2 display up-regulation in the Runx2, OCN, VEGF, BMP-2 expressions compared to Ti and TiO2 on the basis of **Figure 5a**. Moreover, the expression pattern of the key osteogenic genes shows dramatic differences when come to Sr-TiO_2 group. At all-time points, statistically significant mRNA variations are observed when compared the modified group with others.

In the immunofluorescence assay, OCN was detected with DyLight 488 to measure the expression in the cells. **Figure 5b** indicates that modified groups showed stronger immunofluorescence labeling than Ti and TiO_2. More cells expressing the relevant specific protein were detected in the Sr-TiO_2 group.

3.5. Effect of extracts on OVX BMSCs

In the ALP staining test, the positive area was highest in group Sr-TiO_2, while group AT-TiO_2 showed the least intense ALP staining (**Figure 6a**). The intensity of group TiO_2 was less than Sr-TiO_2 but stronger than group Ti. The level of expression of related osteogenic genes by RT-PCR in **Figure 6b** showed that group Sr-TiO_2 has the greatest promotion effect on OCN at day 4, though all groups showed no significant differences in the detection of VEGF gene expression.

3.6. Osteoclast activity

The THP-1 cells matured apparently by the induction of RANKL. The titanium

samples mimicked the real state occurring in the periprosthetic region, which was derived from the implants *in vivo*. Cathepsin K is closely involved in osteoclastic bone resorption and may play an important role in extracellular matrix degradation;[46, 47] its expression relates to the disorder in bone remodeling. **Figure 7** shows the specific protein expression of the cells cultured on different titanium samples. Fully differentiated osteoclast-like cells with numerous nucleuses and localized proteins were detected in cells adhered to the Ti and TiO_2 groups. Distinct colonies of mononuclear cells were found on the AT-TiO_2 and Sr-TiO_2 group. From the figure, the latter showed the least cluster of nucleuses, which means that the osteoclast-like cell density was the lowest among all the samples. In the PCR analysis of the cells on the samples, the CTSK expression showed a correlating trend: the Sr-TiO_2 group presented a lower level when compared to the other groups. The extracts permitted investigation into the effects of Sr ions on the formation and function of osteoclastic cells. Tartrate-resistant acid phosphatase (TRAP) is highly expressed by osteoclasts; accordingly, its expression was evaluated as a marker for the osteoclast phenotype.[48] The figure shows that similar levels of osteoclasts were reached when cultured in the extracts of Ti, TiO_2, and AT-TiO_2. The synthesis of TRAP by osteoclast like-cells was also significantly higher among the three groups in the PCR test. The Sr-TiO_2 group showed less promotion in the TRAP activity and gene expression when compared to the other groups, including the control group. However, due to the lack of induction with the cytokines, the osteoclasts were rarely seen in the blank group, and the related gene expression was also drastically reduced.[49]

3.7. *In Vivo* evaluation

Eight weeks after implantation, all of the groups of implants were extracted from the femur bones and underwent different experiments to test the effect of osseointegration and bone formation. The fluorescent labeling results in **Figure 8a** show that the micro-nano groups exhibited active new bone formation and mineralization during the whole healing period which was indicated by the three fluorescent chromes and further demonstrated by the analysis result in **Figure 8c**. From the van Gieson-stained sections in **Figure 9a** and the corresponding analysis result in **Figure 9b**, significant differences were also found in AT-TiO_2 and Sr-TiO_2 groups when compared with Ti and TiO_2. **Figure 9a** shows that the implants were histologically in direct contact with the surrounding bone, with no signs of inflammation at the bone–implant interface, and the Sr-TiO_2 implant showed a great degree of continuous direct bone apposition and the highest bone-implant contact when compared with the control on the surfaces.

4. Discussion

Among all the medical metallic biomaterials, titanium has been enormously used as implants in dentistry and orthopedics for several decades, which benefit from its good biocompatibility; additional features that make titanium attractive as an implant material are its excellent corrosion resistance, chemical stability and low toxicity in biological environments.[50, 51] To further realize the multifunctional purposes for

clinical applications, such as improving bioactivity, enhancing osteogenesis, promoting osseointegration, there is a growing trend to unite various feasible surface modification methods to biofunctionalize titanium materials. MAO, also named plasma electrolytic oxidation (PEO), is a relatively feasible and cost-effective surface modification strategy for fabricating TiO_2-based coatings on titanium. Increasingly, attention has focused on the biological performances of these oxide coatings on titanium implants, which have manifested its great promise for applications in orthopedic and dental clinical work.[21, 52] In the present work, after alkali treatment, one can see that homogeneous microcracks emerge on the coating surface. Even at a relatively mild condition (low concentration of 0.5 M of NaOH at low temperature of 60 °C), alkali treatment can still result in the appearance of microcracks on oxide coatings.[53] We thus propose that the microcrack formation is mainly due to the thickness of the MAO coatings. In fact, even a sole MAO treatment may also produce tiny microcracks on coatings.[52] To minimize the microcrack formation, a presumably feasible strategy is to micro-arc oxidize titanium species that are pre-patterned below a threshold dimension based on the average size of the microcracks,[54] which is expected to control coating delamination and improve structural strength to some extent for practical applications. However, it is expected that the microcracks can help Sr loading and nutrient element release, and further enhance bone in-growth due to the large structure fluctuation and specific surface area. According to the surface XPS analysis in **Figure 2a-c**, the amounts of Ca and P elements decrease after protonation treatment, *i.e.*, ion exchange in HCl solution. However, this situation is effectively

improved by Sr ion exchange in $SrCl_2$ solution, which increases the contents of Ca and P elements up to approximately one order of magnitude and narrows the gap between samples TiO_2 and Sr-TiO_2 to the same magnitude. Besides, presumably, Ca and P ions are easy to dissolve into an acidic environment while a neutral/basic environment can reduce the ease of Ca/P dissolution and endow with a slow release. On the basis of the release features in **Figure 2g-i**, although Ca and P ions can be released from sample AT-TiO_2 slowly, the total release amounts are the least during the immersion period due to the loss. Nevertheless, the total amounts of Ca/P release from sample TiO_2 do not show much more than sample AT-TiO_2, indicating that the released ions mainly come from the shallow surface of coating rather than the inner layer. It is noteworthy that both Ca and P ions can be sustainably released from sample Sr-TiO_2 at a relatively high rate up to the highest total amounts, which implies that the released ions originate from both the shallow surface and inner surface of the coating. Owing to the successful Sr incorporation into the coating, sample Sr-TiO_2 can controllably release Sr ions into surrounding DMEM in a slow but continuous manner to alter the local microenvironment. After alkali treatment in concentrated NaOH solution, the surface titania was transformed to titanate.[55] Sr^{2+} ions with an ionic radii of 0.11 nm can easily diffuse into the titanate with a larger interlayer space of 0.98 nm and react with the [TiO_6] octahedral layer.[56] This process was promoted by the negatively charged surfaces of titanate layer with a positive affinity to Sr^{2+} cations.[57] After ion exchange process, Na^+ ions with an ionic radii of 0.102 nm were replaced by Sr ions and kept the same geometric [TiO_6] octahedron.[58]

Concerted efforts have been made since the "osseointegration" between bone and implants is found, and the applications of implants grow faster in these years.[59, 60] The number of fractures caused by osteoporosis is expected to increase considerably worldwide, not only because of the increasing number of elderly people in many populations, but also the lack of certain therapeutic interventions. As dental implants will be placed in poor osteoporotic bones, the poor bone quality always enhances the risk of implant failure because the bone resorption process is more rapid than bone formation.[4] The ovariectomized rat (OVX rat) model used in this study to imitate the characteristics of human post-menopausal osteoporosis was verified by the Food and Drug Administration (FDA) as the primary model system to evaluate the prevention and treatment of postmenopausal osteoporosis.[61, 62]

The surface micro/nanostructures on implants not only mimic the structural morphology of constituents of calcified tissues but also resemble the nanocomponents of ECM such as structural proteins and glycosaminoglycans.[63] This type of micro-nano scale topography is critical for imitating the hierarchical structure of natural bones to a certain extent[64] and thus can remarkably enhance the biological properties and improve cell responses.[21] Sr is incorporated into bone by two common mechanisms: (i) a surface exchange involving the incorporation of Sr into the crystal lattice of the bone mineral and (ii) ionic substitution whereby Sr is taken up by ionic exchange with bone Ca.[65] The cell responses to surface topography are the sum of their ability to attach, migrate, proliferate, and differentiate. In the ARS test in **Figure 4a**, the hybrid AT-TiO_2 surface shows a better osteogenic effect than samples Ti and

TiO_2, and Sr-TiO_2 reveals the most calcium nodule in **Figure 4b**. Furthermore, the hybrid surface exhibits a significant enhancement effect on angiogenic expression, and all the gene expressions turned up earlier when compared the results of extracts in **Figure 5a and Figure 6b.** This behavior indicated that the micro-nano surface alone possesses the expected angiogenic and osteogenic effect, and the incorporation of Sr further remarkably promotes the relevant genes expression due to the biological function of Sr.[32, 66] Meanwhile, the results in **Figure 7** also showed that the hybrid AT-TiO_2 and Sr-TiO_2 surfaces possessing a positive effect in inhibiting the osteoclast gene expression and osteoclast activity.

When the implant is inserted into human body, the initial event is that various proteins coming from blood or other tissue fluid adhere onto the surface, including immunoglobulin, fibrinogen, vitronectin, and fibronectin. After protein adhesion, the mesenchymal stem cells (MSCs) and osteoblasts are recruited and cell responses begin.[20] Taking the observations from the systematic test including fluorescence labeling in **Figure 8** and van Gieson staining in **Figure 9** together, all the results show that the modified samples could improve osseointegration, and this is further indicated by calculating the BIC percentage and bone formation area. Moreover, the Sr-TiO_2 group is demonstrated to possess the best angiogenic, osteogenic and osseointegrative effects. On the one hand, the released Sr ions can have promotion effect on bone formation; on the other hand, the high released Ca and P ions can also contribute to the bone formation. These bioactive elements including Sr, Ca and P ions can be released from the implant coating to alter the local microenvironment around living

cells and further promote cell functions and enhance bone formation. To summarize, we suggest that the enhancement of bone formation and osseointegration observed in this study should be a result of the synergistic effect exerted by the hierarchical surface topography and the bioactive Sr, Ca and P ions together. Moreover, from this study it could be concluded that the synergetic effect of strontium element and surface topography is highly significant in achieving enhanced osseointegration and bone growth for implants.

These findings suggest that Sr inhibits osteoclast formation or maturation, which indicates that the Sr-TiO_2 group may inhibit bone resorption and may explain the correlated osseointegration in the *in vivo* model. This phenomenon indicates that the cascade that occurs when Sr-contained titanium implants are present work in the osteoporotic model. However, present study did not clarify the mechanisms in the balance in the *in vivo* implant between osseointegration and bone resorption.[67-70] Despite that these have not been well characterized, an approach presented in the study gives new comprehension to investigations *in vitro* and *in vivo* about the modified implant in the osteoporotic condition.

5. Conclusions

In the present study, a hybrid micro-nano topography with Sr incorporation is fabricated on a titanium surface. The results indicate that the synergetic stimulation of both hierarchical topography and bioactive Sr ions can overall provide a preferential environment for directing OVX BMSC differentiation and possess better osteoblast

compatibility and angiogenesis potential. In addition, cellular gene expression and osteogenic staining demonstrate that the wash-out solution can induce OVX BMSC differentiation similar to the osteogenic stimulation by titanium samples, reflecting the bone formation stimulation of Sr. The differences are obvious at the early stage, indicated by cell adhesion and RT-PCR test, and the advantages remain when staining and immunofluorescence examinations are performed. Furthermore, the Sr presence shows an excellent inhibition effect on osteoclast formation and maturation. The *in vivo* test further indicated that the micro-nano topographical titanium surface incorporated with Sr element could enhance osseointegration in the osteoporotic rat femur model. This study implies that the modified surface with Sr incorporation might be a promising candidate for the revolution of the osseointegration of implants in osteoporotic patients and provides new insights for relevant fundamental investigations and biomedical applications.

Acknowledgements

Joint financial support from the National Basic Research Program of China (973 Program, 2012CB933600), National Science Fund for Distinguished Young Scholars (81225006), Chang Jiang Scholars Program, National Natural Science Foundation of China (81271704, 31370962), and Shanghai Science and Technology R&D Fund (14XD1403900, 13441902400) is acknowledged.

Notes and references

Electronic Supplementary Information (ESI) available. Additional experimental details and results. See DOI:

1. J. A. Kanis, L. J. Melton, C. Christiansen, C. C. Johnston and N. Khaltaev, *Journal of Bone and Mineral Research*, 1994, **9**, 1137-1141.
2. C. Gagnon and P. R. Ebeling, *F1000 medicine reports*, 2009.
3. J. A. Kanis, D. Black, C. Cooper, P. Dargent, B. Dawson-Hughes, C. De Laet, P. Delmas, J. Eisman, O. Johnell, B. Jonsson, L. Melton, A. Oden, S. Papapoulos, H. Pols, R. Rizzoli, A. Silman, A. Tenenhouse, F. Int Osteoporosis and U. S. A. Natl Osteoporosis Fdn, *Osteoporosis International*, 2002, **13**, 527-536.
4. P. J. Meunier, C. Roux, E. Seeman, S. Ortolani, J. E. Badurski, T. D. Spector, J. Cannata, A. Balogh, E.-M. Lemmel, S. Pors-Nielsen, R. Rizzoli, H. K. Genant and J.-Y. Reginster, *New England Journal of Medicine*, 2004, **350**, 459-468.
5. P. J. Marie, M. T. Garba, M. Hott and L. Miravet, *Mineral and Electrolyte Metabolism*, 1985, **11**, 5-13.
6. M. D. Grynpas and P. J. Marie, *Bone*, 1990, **11**, 313-319.
7. S. G. Dahl, P. Allain, P. J. Marie, Y. Mauras, G. Boivin, P. Ammann, Y. Tsouderos, P. D. Delmas and C. Christiansen, *Bone*, 2001, **28**, 446-453.
8. E. Gentleman, Y. C. Fredholm, G. Jell, N. Lotfibakhshaiesh, M. D. O'Donnell,

R. G. Hill and M. M. Stevens, *Biomaterials*, 2010, **31**, 3949-3956.

9. H. Zreiqat, Y. Ramaswamy, C. Wu, A. Paschalidis, Z. Lu, B. James, O. Birke, M. McDonald, D. Little and C. R. Dunstan, *Biomaterials*, 2010, **31**, 3175-3184.

10. J. Forsgren and H. Engqvist, *Journal of materials science. Materials in medicine*, 2010, **21**, 1605-1609.

11. A. S. Nair, P. Zhu, V. Jagadeesh Babu, S. Yang, T. Krishnamoorthy, R. Murugan, S. Peng and S. Ramakrishna, *Langmuir*, 2012, **28**, 6202-6206.

12. A. Sabareeswaran, B. Basu, S. J. Shenoy, Z. Jaffer, N. Saha and A. Stamboulis, *Biomaterials*, 2013, **34**, 9278-9286.

13. Y. Li, Q. Li, S. Zhu, E. Luo, J. Li, G. Feng, Y. Liao and J. Hu, *Biomaterials*, 2010, **31**, 9006-9014.

14. K. Lin, L. Xia, H. Li, X. Jiang, H. Pan, Y. Xu, W. W. Lu, Z. Zhang and J. Chang, *Biomaterials*, 2013, **34**, 10028-10042.

15. Y. Xin, J. Jiang, K. Huo, T. Hu and P. K. Chu, *ACS Nano*, 2009, **3**, 3228-3234.

16. K.-C. Kung, T.-M. Lee and T.-S. Lui, *Journal of Alloys and Compounds*, 2010, **508**, 384-390.

17. L. Zhao, H. Wang, K. Huo, X. Zhang, W. Wang, Y. Zhang, Z. Wu and P. K. Chu, *Biomaterials*, 2013, **34**, 19-29.

18. O. Z. Andersen, V. Offermanns, M. Sillassen, K. P. Almtoft, I. H. Andersen, S. Sørensen, C. S. Jeppesen, D. C. E. Kraft, J. Bøttiger, M. Rasse, F. Kloss and M. Foss, *Biomaterials*, 2013, **34**, 5883-5890.

19. J. Li, W. Zhang, Y. Qiao, H. Zhu, X. Jiang, X. Liu and C. Ding, *Journal of Materials Chemistry B*, 2014, **2**, 283-294.

20. A. Chug, S. Shukla, L. Mahesh and S. Jadwani, *Journal of Oral and Maxillofacial Surgery, Medicine, and Pathology*, 2013, **25**, 1-4.

21. X. Liu, P. K. Chu and C. Ding, *Materials Science and Engineering: R: Reports*, 2010, **70**, 275-302.

22. M. P. Lutolf, P. M. Gilbert and H. M. Blau, *Nature*, 2009, **462**, 433-441.

23. G. Mendonça, D. B. S. Mendonça, F. J. L. Aragão and L. F. Cooper, *Biomaterials*, 2008, **29**, 3822-3835.

24. M. I. Santos, K. Tuzlakoglu, S. Fuchs, M. E. Gomes, K. Peters, R. E. Unger, E. Piskin, R. L. Reis and C. J. Kirkpatrick, *Biomaterials*, 2008, **29**, 4306-4313.

25. M. Liu, C. Wu, Y. Jiao, S. Xiong and C. Zhou, *Journal of Materials Chemistry B*, 2013, **1**, 2078-2089.

26. R. Ng, R. Zang, K. K. Yang, N. Liu and S. T. Yang, *RSC Advances*, 2012, **2**, 10110-10124.

27. Y. Huang, G. Zha, Q. Luo, J. Zhang, F. Zhang, X. Li, S. Zhao, W. Zhu and X. Li, *Sci. Rep.*, 2014, **4**, 6172.

28. J. Li, X. Liu, Y. Qiao, H. Zhu and C. Ding, *Colloids and Surfaces B: Biointerfaces*, 2014, **113**, 134-145.

29. Y. Han, J. Zhou, S. Lu and L. Zhang, *RSC Advances*, 2013, **3**, 11169-11184.

30. H. Yong, Z. Jianhong, Z. Lan and X. Kewei, *Nanotechnology*, 2011, **22**, 275603.

31. J.-W. Park, Y.-J. Kim, J.-H. Jang and J.-Y. Suh, *Journal of Biomedical Materials Research Part A*, 2012, **100A**, 1477-1487.

32. W. Zhang, G. Wang, Y. Liu, X. Zhao, D. Zou, C. Zhu, Y. Jin, Q. Huang, J. Sun, X. Liu, X. Jiang and H. Zreiqat, *Biomaterials*, 2013, **34**, 3184-3195.

33. H. Xie, J. Wang, C. Li, Z. Gu, Q. Chen and L. Li, *Ceramics International*, 2013, **39**, 8945-8954.

34. U. Thormann, S. Ray, U. Sommer, T. Elkhassawna, T. Rehling, M. Hundgeburth, A. Henss, M. Rohnke, J. Janek, K. S. Lips, C. Heiss, G. Schlewitz, G. Szalay, M. Schumacher, M. Gelinsky, R. Schnettler and V. Alt, *Biomaterials*, 2013, **34**, 8589-8598.

35. X. Li, Y. Li, W. Jin, Y. Zheng, C. Rong, H. Lyu and H. Shen, *Nuclear Instruments and Methods in Physics Research Section B: Beam Interactions with Materials and Atoms*, 2014, **332**, 321-325.

36. Q. Shen, D. Zeng, Y. Zhou, L. Xia, Y. Zhao, G. Qiao, L. Xu, Y. Liu, Z. Zhu and X. Jiang, *Journal of Pharmacy and Pharmacology*, 2013, **65**, 1005-1013.

37. X. Jiang, J. Zhao, S. Wang, X. Sun, X. Zhang, J. Chen, D. L. Kaplan and Z. Zhang, *Biomaterials*, 2009, **30**, 4522-4532.

38. A. H. A. Kurth, C. Eberhardt, S. Müller, M. Steinacker, M. Schwarz and F. Bauss, *Bone*, 2005, **37**, 204-210.

39. W. Zhang, Y. Jin, S. Qian, J. Li, Q. Chang, D. Ye, H. Pan, M. Zhang, H. Cao, X. Liu and X. Jiang, *Nanomedicine: Nanotechnology, Biology and Medicine*, 2014, **10**, 1809-1818.

40. J. Li, X. Liu, Y. Qiao, H. Zhu, J. Li, T. Cui and C. Ding, *RSC Advances*, 2013, **3**, 11214-11225.

41. V. V. Divya Rani, K. Manzoor, D. Menon, N. Selvamurugan and S. V. Nair, *Nanotechnology*, 2009, **20**, 195101.

42. Q. Wu, J. Li, W. Zhang, H. Qian, W. She, H. Pan, J. Wen, X. Zhang, X. Liu and X. Jiang, *Journal of Materials Chemistry B*, 2014, **2**, 6738-6748.

43. Y. Han, D. Chen, J. Sun, Y. Zhang and K. Xu, *Acta Biomaterialia*, 2008, **4**, 1518-1529.

44. A. Dupraz, T. P. Nguyen, M. Richard, G. Daculsi and N. Passuti, *Biomaterials*, 1999, **20**, 663-673.

45. J. Li, G. Wang, D. Wang, Q. Wu, X. Jiang and X. Liu, *Journal of Colloid and Interface Science*, 2014, **436**, 160-170.

46. J. Xiong, M. Onal, R. L. Jilka, R. S. Weinstein, S. C. Manolagas and C. A. O'Brien, *Nat Med*, 2011, **17**, 1235-1241.

47. B. Yu, J. Chang, Y. Liu, J. Li, K. Kevork, K. Al-Hezaimi, D. T. Graves, N.-H. Park and C.-Y. Wang, *Nat Med*, 2014, **20**, 1009-1017.

48. X. Flecher, C. Rolland, E. Rixrath, J.-N. Argenson, P. Robert, P. Bongrand, S. Wendling and J. Vitte, *Journal of Clinical Immunology*, 2009, **29**, 681-690.

49. D. Bylski, C. Wedemeyer, J. Xu, T. Sterner, F. Loeer and M. von Knoch, *Journal of Biomedical Materials Research Part A*, 2009, **89A**, 707-716.

50. X. Liu, P. K. Chu and C. Ding, *Materials Science and Engineering: R: Reports*, 2004, **47**, 49-121.

51. M. Geetha, A. K. Singh, R. Asokamani and A. K. Gogia, *Progress in Materials Science*, 2009, **54**, 397-425.

52. A. Krzakala, A. Kazek-Kesik and W. Simka, *RSC Advances*, 2013, **3**, 19725-19743.

53. H. Gao, Y. F. Jie, Z. Q. Wang, H. Wan, L. Gong, R. C. Lu, Y. K. Xue, D. Li, H. Y. Wang, L. N. Hao and Y. Z. Zhang, *Journal of Materials Chemistry B*, 2014, **2**, 1216-1224.

54. A. S. Zuruzi and N. C. MacDonald, *Adv. Funct. Mater.*, 2005, **15**, 396-402.

55. R. Ma, T. Sasaki and Y. Bando, *Journal of the American Chemical Society*, 2004, **126**, 10382-10388.

56. M. Miyauchi, *The Journal of Physical Chemistry C*, 2007, **111**, 12440-12445.

57. H. Tokudome and M. Miyauchi, *Chemical Communications*, 2004, **0**, 958-959.

58. T. P. Feist and P. K. Davies, *Journal of Solid State Chemistry*, 1992, **101**, 275-295.

59. P. Brnemark, *Tissueintegrated prostheses: osseointegration in clinical dentistry. Chicago: Quintessence Publ. Co*, 1985, 11-76.

60. P. Branemark, *Institute for Applied Biotechnology*, 1990.

61. A. S. Turner, *Eur Cell Mater*, 2001, **1**, 13.

62. Food and D. Administration, *Division of Metabolism and Endocrine Drug Products, Rockville, MD*, 1994.

63. S. Sowmya, J. D. Bumgardener, K. P. Chennazhi, S. V. Nair and R. Jayakumar, *Progress in Polymer Science*, 2013, **38**, 1748-1772.

64. L. Feng, S. Li, Y. Li, H. Li, L. Zhang, J. Zhai, Y. Song, B. Liu, L. Jiang and D. Zhu, *Adv. Mater.*, 2002, **14**, 1857-1860.

65. A. P. Dahl S G, Marie P J, et al., *Bone*, 2001, **28(4)**, 446-453.

66. C. J. Chung and H. Y. Long, *Acta biomaterialia*, 2011, **7**, 4081-4087.

67. P. Marie, P. Ammann, G. Boivin and C. Rey, *Calcified tissue international*, 2001, **69**, 121-129.

68. S. Peng, X. S. Liu, S. Huang, Z. Li, H. Pan, W. Zhen, K. D. K. Luk, X. E. Guo and W. W. Lu, *Bone*, 2011, **49**, 1290-1298.

69. Z. Saidak and P. J. Marie, *Pharmacology & Therapeutics*, 2012, **136**, 216-226.

70. M. Roy and S. Bose, *Journal of Biomedical Materials Research Part A*, 2012, **100A**, 2450-2461.

Table 1. Primers for real-time polymerase chain reaction (PCR).

Gene	Prime sequence (F, forward; R, reverse)	Product size (bp)	Accession number
β-Actin	F: AGGGAGTGATGGTTGGAATG	107	NM_031004.2
	R: GATGATGCCGTGTTCTATCG		
RUNX2	F: CCGAGACCAACCGAGTCATT	114	NM_001278483.1
	R: CACTGCACTGAAGAGGCTGT		
OCN	F:CAGTAAGGTGGTGAATAGACTCCG	172	NM_013414.1
	R: GGTGCCATAGATGCGCTTG		
BMP-2	F: ATGGGTTTGTGGTGGAAGTG	167	NM_017178.1
	R: TGTTTGTGGAGTGGATGTC		
VEGF	F: TTGAGTTGGGAGGAGGATGT	115	NM_001110333.1
	R: TGGCAGGCAAACAGACTTC		
CTSK	F: CTGGCTATGAACCACCTGGG	102	NM_000396.3
	R: AAGGGTGTCATTACTGCGGG		
TRAP	F: AGTGGCCTCAGCGTTGAATG	130	NM_001111034.1
	R: TTTATTCCCTCCCTGCCTGC		

Figure captions

Figure 1. Surface morphology of the samples Ti (**a-b**), TiO_2 (**c-d**), AT-TiO_2 (**e-f**), and Sr-TiO_2 (**g-h**) examined by SEM at low and high magnifications. The insets are the corresponding further magnified topographies.

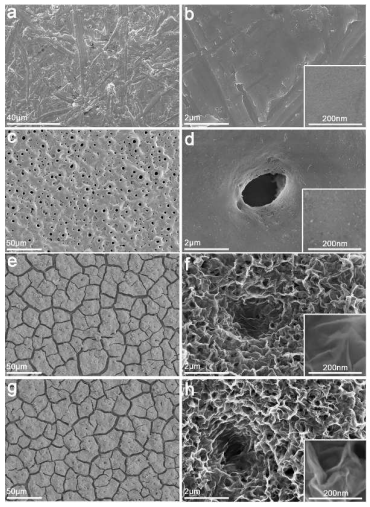

Figure 2. Surface XPS full spectra of the samples TiO_2 (**a**), AT-TiO_2 (**b**), and Sr-TiO_2 (**c**), High-resolution XPS spectra of Ca 2p (**d**), P 2p (**e**) and Sr 3d (**f**), accompanied by the release characteristics of Ca (**g**), P (**h**) and Sr (**i**) ions. Note: no Sr ions were released from samples TiO_2 and AT-TiO_2 with overlap of release curves.

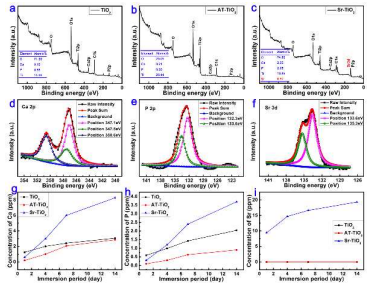

Figure 3. OVX BMSC proliferation and adhesion. (**a**) CCK8 assay for cell viability and proliferation on the sample surfaces at days 1, 4 and 7. (**b**) Immunofluorescence detection of cells morphology examined by confocal laser scanning microscope at 12 hours and 24 hours, showing the adhesion and spreading abilities. (*p< 0.05, ***p < 0.001)

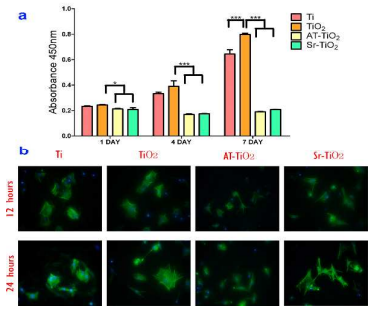

Figure 4. Staining and semiquantitative analysis of ALP and ARS activities. (**a**) ALP staining of OVX BMSCs cultured on the surfaces at day 7 and ARS staining of OVX BMSCs cultured on the surfaces at day 14. (**b**) Semiquantitative assay analysis of ALP activity and ARS activity. (**p < 0.01, ***p < 0.001)

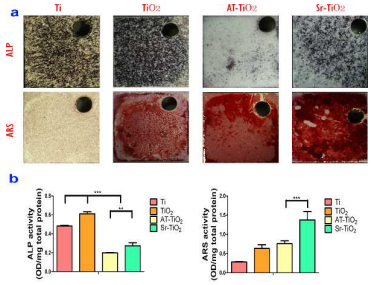

Figure 5. Detection of osteogenic differentiation and OCN expression. (**a**) mRNA expression levels of Runx2, OCN, BMP-2 and VEGF at days 1 and 4, showing the angiogenic and osteogenic activities. (**b**) Immunofluorescence detection of OCN expression at day 4. (*p < 0.05, **p < 0.01, ***p < 0.001)

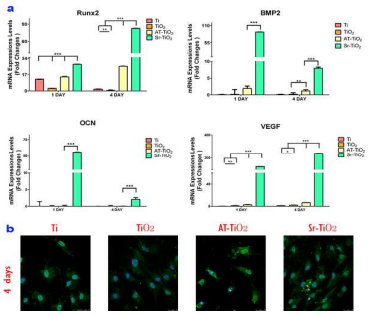

Figure 6. Detection of osteogenic differentiation induced by extracts. (**a**) ALP staining and semiquantitative analysis of ALP activity at days 1 and 4. (**b**) mRNA expression levels of OCN and VEGF at day 1 and 4, showing the angiogenic and osteogenic activities. (***p < 0.001)

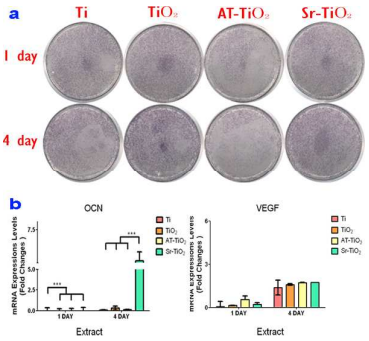

Figure 7. Osteoclasts detection and differentiation. (**a**) Immunofluorescence detection (Green: CTSK, Blue: DAPI) and (**b**) mRNA expression levels of CTSK on the titanium samples at day 5. Trap staining (**c**) and mRNA expression levels (**d**) of the

extracts. (*p < 0.05, **p < 0.01, ***p < 0.001)

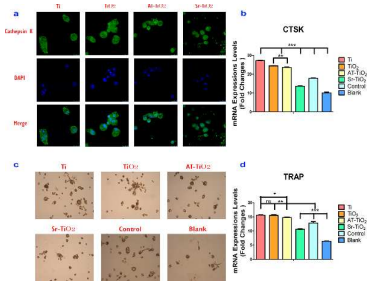

Figure 8. Sequential fluorescent labeling observation and analysis. (**a**) Red, yellow and green represent labeling by Alizarin Red S (AL, week 2), tetracycline (TE, week 4) and calcein (CA, week 6), respectively. Scale bar: 100 μm. (**b**) The image shows the blue rectangle region that was selected to evaluate the formation rate of new bone. (**c**) Analysis of the area of bone stained with the three fluorochromes. (***p < 0.001)

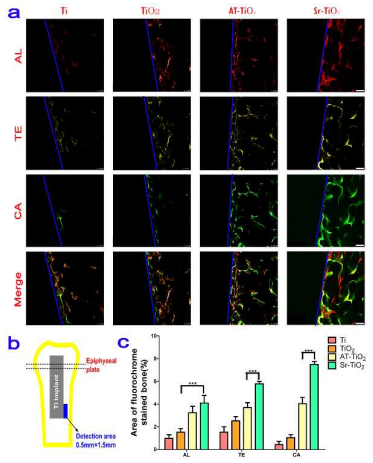

Figure 9. Histological observation and analysis on the samples collected at week 8 after surgery. (**a**) Histomorphometric observation stained with van Gieson's picrofuchsin. The 100X images correspond to the partially magnified blue rectangle areas in 12.5X images. (**b**) Analysis of BIC from the histomorphometric

measurements. (***$p < 0.001$)

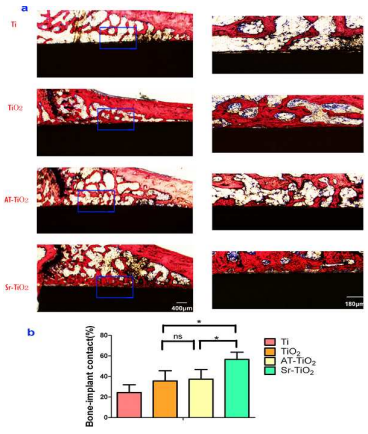

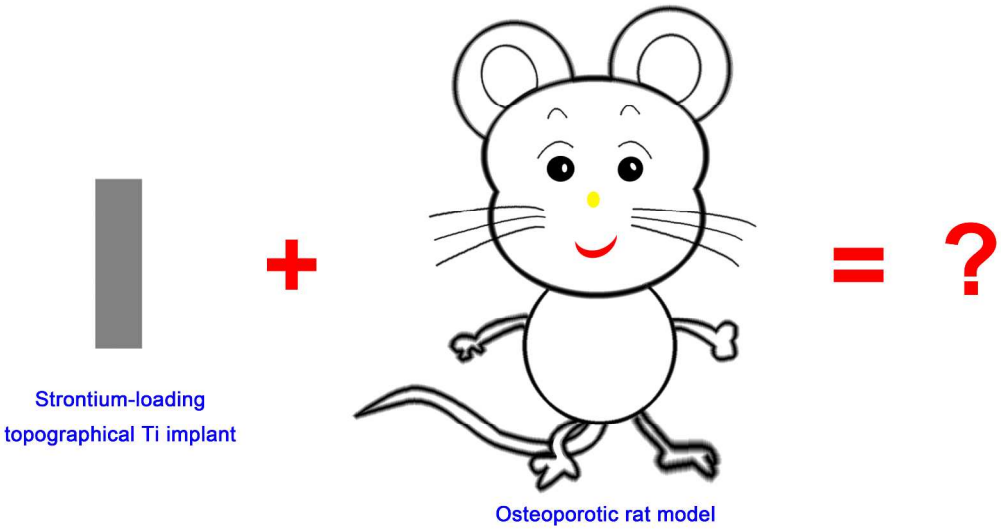

Strontium-substitued hierarchical Ti surface can enhance the osseointegration by both increasing new bone formation and reducing bone resorption under osteoporotic conditions.

1716x915mm (72 x 72 DPI)